GIG Research Institute

JOURNAL OF SUSTAINABLE MINING

Volume 21 | Issue 3 Article 6

2022

Panel Destressing Strategies for Remnant Pillar Extraction

Author(s) ORCID Identifier:
Isaac Vennes: 0000-0001-7737-7154
Hani Mitri: 0000-0002-6482-7424

Panel Destressing Strategies for Remnant Pillar Extraction

Abstract

Large-scale panel destressing is a rockburst mitigation technique employed in deep hard rock mines during remnant pillar extraction. Panels are choke blasted in the pillar footwall to cutoff the far-field major stress in the mining area and deviate them around the pillar. In this study, the effects of panel geometry and far-field stress magnitude are investigated. Destress blast performance is assessed by measuring change to the energy release rate (ERR) of all mining steps during the extraction of a simplified remnant pillar due to destressing. It is demonstrated that the energy release rate (ERR) of critical stopes is reduced by 30% with the base panel geometry. The panel thickness is shown to have the most influence on the efficiency of destressing, followed by the stand-off distance between the panel and the pillar and the overhang length of the panel. The effect of far-field stress magnitude on the ERR is also investigated, and the destress blast performance is expressed as an equivalent major principal stress reduction. It is shown that with the base panel geometry, the destressing program offers the same ERR reduction as a 9.6 MPa reduction in the far-field stress for the most critical stopes. Finally, the Copper Cliff Mine (CCM) panel destressing program is presented as a case study. The ore at risk and ERR are calculated over the extraction and destressing sequence in the pillar with a pillar-wide numerical model.

Keywords

destress blasting, pre-conditioning, rockbursts, numerical modelling

RESEARCH ARTICLE

Panel Destressing Strategies for Remnant Pillar Extraction

Isaac Vennes*, Hani Mitri

McGill University, Department of Mining and Materials Engineering, 3450 University Street, Montreal, Quebec, Canada

Abstract

Large-scale panel destressing is a rockburst mitigation technique employed in deep hard rock mines during remnant pillar extraction. Panels are choke blasted in the pillar footwall to cutoff the far-field major stress in the mining area and deviate them around the pillar. In this study, the effects of panel geometry and far-field stress magnitude are investigated. Destress blast performance is assessed by measuring change to the energy release rate (ERR) of all mining steps during the extraction of a simplified remnant pillar due to destressing. It is demonstrated that the energy release rate (ERR) of critical stopes is reduced by 30% with the base panel geometry. The panel thickness is shown to have the most influence on the efficiency of destressing, followed by the stand-off distance between the panel and the pillar and the overhang length of the panel. The effect of far-field stress magnitude on the ERR is also investigated, and the destress blast performance is expressed as an equivalent major principal stress reduction. It is shown that with the base panel geometry, the destressing program offers the same ERR reduction as a 9.6 MPa reduction in the far-field stress for the most critical stopes. Finally, the Copper Cliff Mine (CCM) panel destressing program is presented as a case study. The ore at risk and ERR are calculated over the extraction and destressing sequence in the pillar with a pillar-wide numerical model.

Keywords: destress blasting, pre-conditioning, rockbursts, numerical modelling

1. Introduction

Rockbursts occur when brittle rock is loaded beyond its failure point, manifesting as a sudden and violent failure. Contributing factors to the occurrence of rockbursts are high stress, stiff strata, rapid mining rate, and large excavation area, among others. Although the mechanisms of rockbursts are well understood and the rockburst risk can be evaluated, rockbursts are still unpredictable. Therefore, once the risk of bursting is apparent, it is necessary to either reduce the rockburst risk or mitigate the damage of an eventual rockburst. Destress blasting, also known as ground pre-conditioning, is one of several well-established techniques for rockburst control in underground coal and hard rock mines. In general, the technique aims to reduce the risk of rockburst by damaging burst-prone rock in advance of mining or development with explosives. The blast-induced damage in the targeted rock reduces its burstability in multiple ways. First, fracturing reduces the stiffness of the rock as well as its load bearing capacity [1]. Second, strain energy is consumed to fracture the rock, reducing the stored elastic strain energy available for bursting [2]. Finally, the rock undergoes plastic strain, reducing its brittleness [3].

Destress blasting is generally applied in three scenarios: pillar destressing, roof destressing, and drift face destressing. Among these three applications, the analysis of destress blasting-induced damage is mostly conducted in the context of drift development. In this case, destress blast holes are detonated in advance and ahead of the development holes. The blasthole pattern is relatively sparse, and the powder factor per mass of targeted rock is low. Two simulation methods are employed in these studies. First, blast damage models are employed to damage the rock and redistribute stresses around the blast holes and drift face.

Received 11 February 2022; revised 2 June 2022; accepted 4 June 2022.
Available online 18 November 2022

* Corresponding author.
E-mail address: isaac.vennes@mail.mcgill.ca (I. Vennes).

https://doi.org/10.46873/2300-3960.1362

Second, the size of the borehole blast-induced damage zones is assumed, and the holistic effect of detonation on the rock mass, such as stress and young's modulus reduction, is applied to this damage zone.

To begin, Zhu et al. [4] demonstrated the alleviation of the stress concentration ahead of the face due to blast damage with a coupled multi-physical model for the interaction between blasting damage and a coal gas flow. The nominal stress along the strike of the drift ahead of the face is reduced by up to 50%. Furthermore, Sainoki et al. [5] applied the holistic effect of destressing at the face as well as a dynamic blast damage model and showed that with the sparse destress blast hole pattern employed for drift development, the holistic method is overly optimistic. However, Baranowski et al. [6] confirmed the ability of modelling to match the PPV with experimental outcomes. The JWL equation of state was employed for the explosives, and the Johnson Holmquist II (JH-2) constitutive model was used for the rock. Finally, Yu et al. [7] modelled the holistic effect of destressing, namely Young's modulus decrease and Poisson's ratio increase, in the blast damage zones of individual destress blast holes. The stress hazard for different schemes was evaluated based on the elastic strain energy density in the rock.

Panel destress blasting is a destressing strategy applied in deep hard rock mines to facilitate remnant pillar extraction with sublevel open-stoping mining methods. A large panel close to the stope hanging wall is choke-blasted to cut off the principal stress under which the stope pillar is subjected. Access to the panel is achieved by extending the stope sill drive into the hanging wall of the remnant stope. Panel blasting prior to stope mining helps create a stress shadow in the stope pillar. Two factors contribute to the stress shadow effect. First, the reduction of the panel's Young's modulus due to blasting-induced damage reduces the stiffness of the panel relative to the surrounding rock mass. Second, the stored strain energy in the rock is consumed during the damage process [2], reducing the magnitude of the stress-tensor in the panel. These two effects generate the stress shadow shown in Fig. 1.

Three case studies report the use of large-scale panel destressing in hard rock Canadian Mines: Brunswick Mine [9], Fraser Mine [10], and Copper Cliff Mine [11]. Table 1 summarizes the blasting pattern for the panels. The panel geometries are provided in Table 2. The targeted mass, M_e, is calculated based on the blasthole diameter:

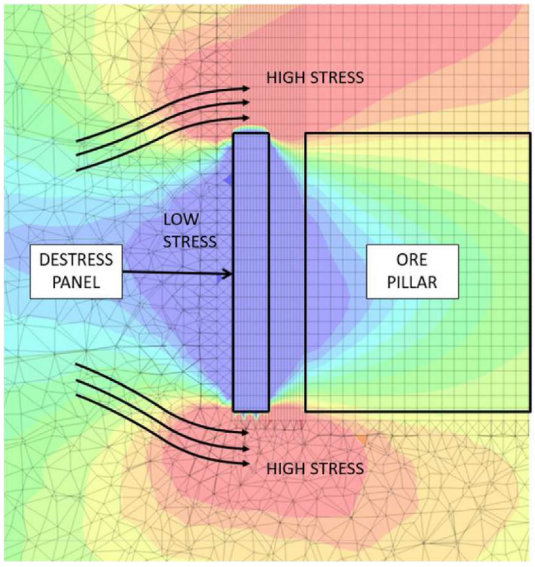

Fig. 1. Stress shadow effect around destress panel [8].

$$M_e = 2(16d)HL\rho_r \quad (1)$$

where d is the blasthole diameter, H is the panel height, L is the length, and ρ_r is the density of the rock.

Overall, the case study panels have a targeted mass ranging from 10 Kt to 30 Kt, with a blasthole pattern consisting of two rows of large diameter blastholes. The explosive energy per targeted mass is relatively high compared with other destressing forms such as drift face-conditioning and longwall roof destressing. For instance, Phase 1 destress blast at CCM yielded an explosive energy density of 500 cal per kg of panel mass. This is in accordance with the Fraser and Brunswick Mine case studies, where the panel explosive energy densities were 500 cal/kg and 200 cal/kg, respectively. On the other hand, the explosive energy of tactical blasts ranges between 10 cal/kg and 100 cal/kg [10].

The relatively high panel explosive energy density partially explains the severe blasting-induced damage in the panel. For instance, for the Phase 1 blast at CCM, Young's modulus and stress tensor in the targeted mass were both reduced by 95% to match the measured stress changes in the stress shadow. For Brunswick mine, measured and computed stress changes with a 3DEC model matched when the panel was extracted from the model, equivalent to a 100% panel elasticity and stress [10]. On the other hand, the blast-induced damage effect for face pre-conditioning is estimated at 40–60% [2,5,7].

To begin, the effect of panel size and distance from the mining zone has not been assessed. Given

Table 1. Panel destressing case study blast parameters.

Mine		Blasthole diameter (mm)	Toe spacing (m)	Hole length (m)	Average charge length (m)	Maximum Charge per delay (kg)	Pattern
Brunswick Mine [9]		165	2.4	27[a]	20	607	32 holes in two rows, along strike of drift parallel to orebody strike, 45° downwards
Fraser Mine [10]		114	3	23[a]	13	473	28 holes in two rows, fanned from drift perpendicular to orebody strike
Copper Cliff Mine	Phase 1 [11]	114	2.6	6–32	15.2	223	180 holes in two rows, fanned parallel to orebody strike from three drifts
	Phase 3 [12]	114	2.8	5–36	24.2	306	120 holes in two rows, fanned parallel to orebody strike from two drifts

[a] Average hole length.

Table 2. Case study panel geometry.

Mine		Width (m)	Height (m)	Thickness (m)	Targeted Mass (Kt)
Brunswick Mine [9]		30	27	5.3	27
Fraser Mine [10]		18	27.5	3.6	10
Copper Cliff Mine	Phase 1 [11]	32	78	3.6	30
	Phase 3 [12]	36	75	3.6	26

that numerical modelling back analysis case studies have shown that reducing the panel stiffness and stress can replicate the stress changes measured in the field and that the application of these two effects in the model provides an immediate beneficial stress reduction in the stress shadow stopes [11,12], it is possible to simulate different panel sizes and distances in a simplified pillar model. Moreover, the benefit of destressing can be quantified with the model over the entire extraction sequence of the remnant pillar to assess the effect of panel geometry.

Next, a suitable burstability criterion must be applied to the pillar to assess the benefit of destressing. Despite the high blasting-induced fragmentation and stress reduction in the panel, the benefits of large-scale panel destressing are not immediately apparent if only the stress decrease in the panel shadow is considered. The measured stress reduction in the stress shadow for all panel case studies is relatively small compared to premining stresses [11]. However, other pillar burstability assessment criteria such as volume of ore at risk [13] and energy release rate (ERR) [14] elucidate the benefits of destressing when applied to a remnant pillar numerical analysis. Therefore, the effect of panel geometry will be assessed with the ERR, with the anticipation that the destress panel will reduce the ERR of subsequent mining steps. It is also beneficial to equate the computed ERR changes to a stress change since stress changes are easier to interpret. To achieve this, the equivalent far-field stress change criterion is developed, where the criterion equates the effect of destressing to the effect of reducing the far-field stress on the mining step ERR. With this methodology, it is possible to express the benefit of a destress panel to a stope as a single stress change value.

The pillar-wide numerical model is constructed in FLAC3D. Since ERR involves the calculated stored elastic strain energies, the linear-elastic constitutive model is suitable for the study. The holistic effect of destressing is simulated with the rock fragmentation factor (α) and stress dissipation factor (β) in the panel zones, representing the instantaneous decrease in elastic modulus and stress tensor, respectively. The fragmentation and stress reduction parameters validated by Vennes et al. [11] are employed.

2. Parametric study setup

2.1. Simulation of destress blasting

To generate a stress shadow, the holistic effect of destressing, specifically the stress reduction and stiffness reduction due to blasting-induced damage, will be applied to the panel. The Young's modulus is reduced, and Poisson's ratio is increased. These two

effects are implemented in the model with the fragmentation factor α. The instantaneous reduction of stresses is also applied with the stress reduction factor β. Once these parameters are applied to panel zones and the model is solved, a stress shadow is generated around the panel, redistributing stress around the remnant pillar. This simulation method was validated using stress change data from the panel destressing program at Copper Cliff Mine [11,12]. Based on the first panel in the sequence, it was found that an isotropic reduction of 95% for both the stress tensor and elasticity adequately replicated the measured stress changed in the remnant ore pillar (α = 0.05, β = 0.95). For the second and third panels however, it was demonstrated that an anisotropic reduction of panel stresses and Young's modulus corroborated with the measured stress changes, which can be attributed to preferential fracture propagation in the direction of the major principal stress. In this study, the validated parameters for the first panel at CCM will be employed, representing an ideal blast providing maximal stress relief in the stress shadow. Moreover, the parameters remain constant for all destressing phases. The rock fragmentation factor and stress reduction factors are applied to the model following Equations (2)–(5) [2].

$$E_{destress} = E\alpha \tag{2}$$

$$\upsilon_{\text{destress}} = \upsilon^{*}(2-\alpha) < 0.5 \tag{3}$$

$$\{\sigma_{\text{D}}\} = (1-\beta)\cdot\{\sigma\} \tag{4}$$

$$\{\sigma\} = \left(\sigma_{xx}, \sigma_{yy}, \sigma_{zz}, \sigma_{xy}, \sigma_{yz}, \sigma_{xz}\right) \tag{5}$$

2.2. Model construction

A three-dimensional model of the remnant pillar is constructed in FLAC3D and solved with the finite difference procedure. The entire pillar destressing and extraction sequence is simulated, along with the pillar formation sequence. The pillar extraction sequence is illustrated in Fig. 2. The pillar is composed of 16 stopes on two levels, with four stopes along the strike and two stopes along the thickness. The stope dimensions are 10 m × 10 m × 20 m (width × strike length × height). The panels are placed in the hanging wall of the remnant pillar. Destressing is done in four steps, with one panel per step. Together, the four panels cover the entirety of the remnant pillar hanging wall. Fig. 3 shows the geometry of the pillar and the four modelled panels.

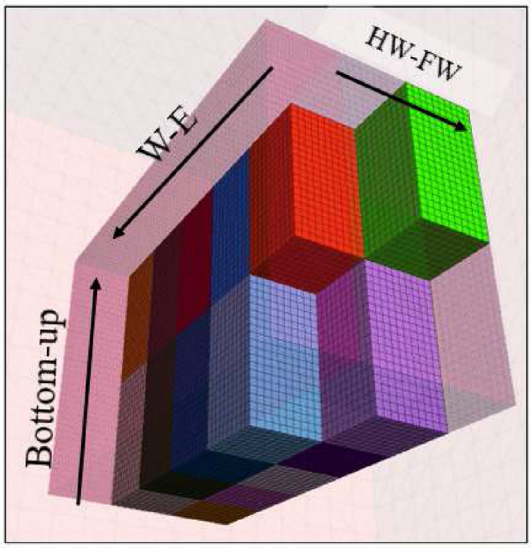

Fig. 2. Remnant pillar extraction sequence.

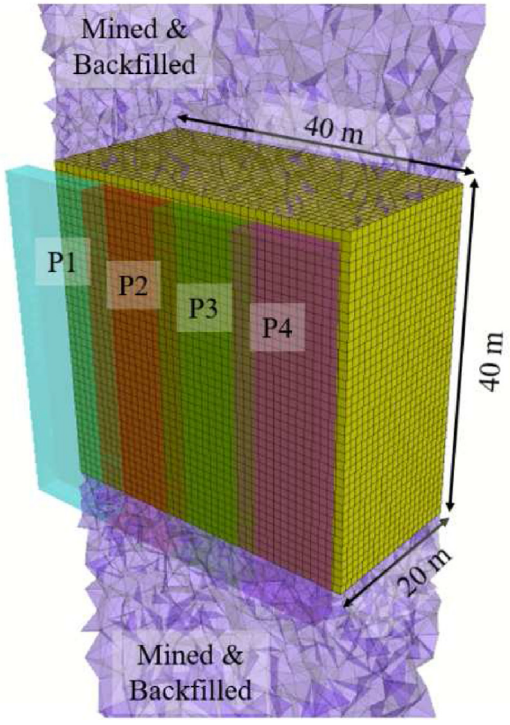

Fig. 3. Remnant pillar geometry and destress panel sequence.

Table 3. Model material properties.

Material	Elastic properties			
	E_{intact} (GPa)	E_{rockmass} (GPa)	ν	γ (kN/m^3)
Host rock	48	24.96	0.18	28.5
Orebody	52	27.6	0.19	36.3
Backfill	N/A	2	0.3	20

The model is composed of three material types, all modelled as linear elastic. The material properties provided in Table 3 recreate the rock masses encountered at CCM, where a large-scale panel destressing program was implemented. Both the footwall and hanging wall of the orebody are composed of the same rock type. No other geological structures are included.

The model is loaded by applying pressure on the outer boundaries, allowing for the calculation of boundary work due to changing model geometry during stope extraction and destressing. The applied pressures are calibrated to account for the model body forces and match the Sudbury regional stresses equations (Equations (6)–(8)) across a vertical centerline running down the model.

$$\sigma_1 = 10.82 + 0.0407D \tag{6}$$

$$\sigma_2 = 8.62 + 0.0326D \tag{7}$$

$$\sigma_3 = 0.0292D \tag{8}$$

where D is the depth in meters, and the stress is in MPa. The major principal stress (σ_1) is horizontal and applied to the model boundary faces parallel to the orebody strike, such that the major stress is perpendicular to the orebody strike. The intermediate stress (σ_2) is also horizontal and parallel to the orebody strike. The minor stress (σ_3) is vertical. The remnant pillar is modelled at a depth of 1 km.

The orebody above and below the remnant pillar is extracted in 10 m lifts with a bottom-up mining sequence. The excavated zones are immediately replaced with backfill material after each lift. Next, the pillar is extracted following a West to East, bottom up, hanging wall to footwall mining sequence. In terms of sequencing, the stopes at the hanging wall contact are the primary stopes, and the stopes at the footwall contact are the secondary stopes. All cavities are immediately replaced with backfill material after solving. Fig. 2 shows the mining front of the pillar following this sequence. Destressing is implemented in conjunction with the stope extraction sequence, such that all stopes are under a stress shadow once extracted. For example, before mining the first stope in the pillar, panel 1 will be destressed, providing this stope with a stress shadow. Panel 2 will then only be destressed once the extraction sequence reaches the next stope along the strike. Consequently, the pillar is fully destressed well ahead of the full retrieval of the pillar; in this instance, the last panel is blasted before the extraction of the ninth stope out of the 16 stopes in the pillar.

2.3. Assessment of destress blast efficiency

There are three popular methods employed in the literature to evaluate destress blast efficiency with field measurements. First, the seismic activity before and after a destress blast is compared, where a decrease of seismic event frequency and magnitude is anticipated in the destressed zone. This method is exemplified by Drover et al. [15], who demonstrated a significant difference in seismic activity ahead of two advancing parallel tunnels, one with pre-conditioning at the face and one without. Second, the measurement of destress blast seismic source parameters such as the seismic efficiency (SE) and moment tensor is a proven technique for the assessment of destress blast efficiency [16–18]. Third, stress changes are measured, where lower stress is anticipated in the destressed zone and where the risk posed by future seismic activity is related to the magnitude of these stresses. Unlike the two former methods, destressing efficiency assessment using induced stress changes can be easily conducted with a numerical model. However, to evaluate the benefit of the destress blast, a suitable rockburst potential indicator is needed. With the indicator, the effect of a destress blast can be quantified based on the stress difference between a mining sequence with destressing and a sequence with no destressing. Among others, applicable criteria include the brittle shear ratio [19] or the burst potential index [14]. With these burst criteria, the effect of destressing-induced stress changes on rockburst risk can be established.

In the field, a significant stress reduction in destress panel stress shadows was measured at Brunswick Mine [9] and Fraser Mine [10] with uniaxial vibrating wire stress cells. Along with a comparison of seismic activity before and after destressing in the pillar, the panel destressing program was deemed successful in both cases. At Copper Cliff Mine, ten uniaxial vibrating wire stress cells were installed in the remnant pillar. Stress relaxation was captured with stress cells directly in the panel stress shadow, and the destress blast holistic effect was validated with a pillar-wide linear elastic model [11,12]. Similarly, Konicek et al. [20] employed compact conical-ended borehole monitoring (CCBM) probes to measure the stress tensor in the longwall roof before and after destressing, and the impact of destressing was identifiable.

Given a measured or computed stress change, the effect of this stress change on burst risk must be quantified. Multiple stress-based and energy-based criteria are described in the literature. The brittle shear ratio proposed by Castro et al. [19] is the ratio

between the deviatoric stress in the rock and the intact UCS, where damage initiates at a ratio of 0.4, and the rock is at risk of brittle failure at a ratio of 0.7. Shnorhokian et al. [13] demonstrated spatial relation between the BSR and the location of seismicity and developed the ore at risk criterion to assess stope sequencing alternatives to reduce bursting. Furthermore, Vennes et al. [8] employed the ore at risk criterion in a destress blasting parametric study, where ore at risk was defined as the volume of rock with a BSR greater than 0.7. It was found that panel destressing significantly reduced the volume of ore at risk in the pillar; since the pillar was close to failure, a 5% decrease in the major principal stress was sufficient to reduce the ore at risk volume by a factor of 2. Alternatively, the stored strain energy in the rock can be calculated based on the stress tensor and elastic strain tensor. For example, the burst potential index (BPI) developed by Mitri et al. [14] measures the ratio between the current strain energy in the rock and the critical strain energy at failure. Finally, the change in stored strain energy over time can be used to assess the risk of bursting. The energy release rate (ERR) [21] describes the elastic energy per volume that is released when a geometrical change in the rock, such as an excavation, occurs. Its counterpart, the energy storage rate (ESR) measured the stored strain energy in the rock. Fig. 4 shows a graphical representation of the ERR and the ESR for a mining step. Qinghua et al. [22] developed two similar indices: the local energy release rate (LEER) and the fractional energy release rate (FERR), to evaluate the risk of rockburst. The LEER captures the energy released at a certain element in a numerical model. The spatial distribution of energy release can therefore be determined. Furthermore, the FERR was developed to allow rock failure to be considered.

In this study, destress blast efficiency will be assessed with the ERR. It is demonstrated that mining in smaller step reduces the released seismic energy, which must cause a seismic effect [14]. A similar analysis can be conducted for destressing, where the ERR extraction steps in a destress pillar are anticipated to be lower, in effect providing a similar benefit to mining in smaller steps. ERR is therefore a suitable criterion for this comparative study between a mining scenario with destressing and without destressing. The ERR is calculated in the model by measuring the boundary work on the model for each mining step. The difference in work between each step is then accounted for equal parts between ERR_i and ΔESR_i. The boundary work "W" on the model is calculated as:

$$W = \sum_{i=1}^{n} A_i \left(U_{i,x} \left(\sigma_{i,x} + \sigma_{i,xy} \right) + U_{i,y} \left(\sigma_{i,y} + \sigma_{i,xy} \right) + U_{i,z} \sigma_{i,z} \right) \tag{9}$$

where for a total of "n" boundary faces, and for a given boundary face "i", A_i is the area, $U_{i,x}$ is the displacement at the face center in the "x" direction, and $\sigma_{i,x}$ is pressure applied to the boundary face in the "x" direction.

2.4. Varied geometric parameters

Three panel geometry parameters are varied, namely the panel thickness, the panel standoff, and the panel overhang (see Fig. 5). The tested parameter combinations are selected following the central composite design (CCD) method (see Fig. 6), which

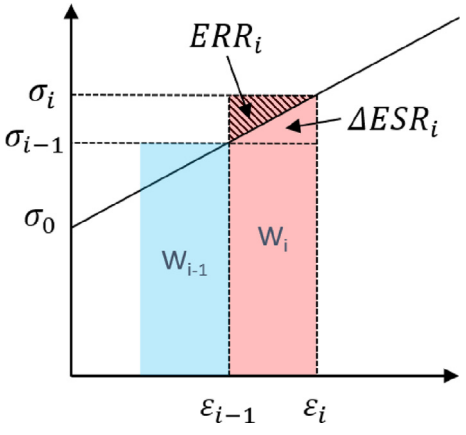

Fig. 4. Energy components of mining step "i".

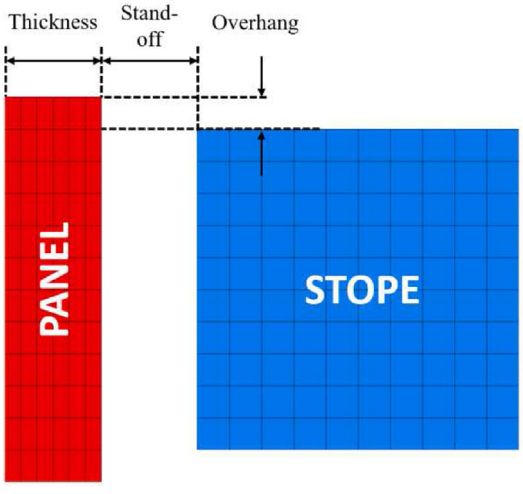

Fig. 5. Varied geometric parameters.

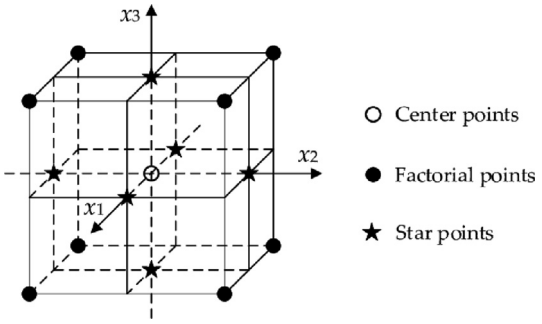

Fig. 6. Central composite design combinations with three varied parameters [23].

generates 15 combinations of parameters (points). The centre point is a model with all geometric parameters set at their base values. The factorial points are all possible combinations of extreme values, which can be mapped to the corners of a cube. Finally, the star points vary a single parameter between the two extremes, while keeping the other two at their base value. All tested combinations are provided in Table 4.

Moreover, the magnitude of the major stress is varied using the center point model to calculate the equivalent major principal stress change caused by destressing. Three different stress regimes were applied to the base model: Tectonic stress, mid-stress, and hydrostatic stress. Table 5 summarizes the major stress at the model center for the three tested stress regimes. Note that the base stress regime was used for all models where destressing was simulated.

Table 4. Parametric study models.

	Model name	Standoff (m)	Thickness (m)	Overhang (m)
Center	p000	3	3	1
Factorial points	p--+	4	1.5	2
	p-++	4	4.5	2
	p+-+	2	1.5	2
	p+++	2	4.5	2
	p---	4	1.5	0
	p-+-	4	4.5	0
	p+--	2	1.5	0
	p++-	2	4.5	0
Star points	p-00	4	3	1
	p+00	2	3	1
	p0-0	3	1.5	1
	p0+0	3	4.5	1
	p00+	3	3	2
	p00-	3	3	0

Table 5. Tested far-field stress scenarios with no destressing in sequence.

Far-field stress Regime	Major stresses at model center (MPa)		
	σ_1 N-S	σ_2 E-W	σ_3 z
Base	51	41	29
Mid-stress	46	41	29
Min-stress	41	41	29

3. Parametric study results

3.1. Variation of far-field stresses

The remnant pillar extraction sequence was implemented without destressing in the model with varying far-field stress regimes. In the base stress regime, the Sudbury regional stress equations are matched at the remnant pillar depth. The major principal stress is 51 MPa, in the horizontal direction perpendicular to the strike of the pillar. The intermediate stress, horizontal and parallel to the strike, is 41 MPa. Finally, the minor stress in the vertical direction, has a magnitude of 29 MPa. In the min-stress regime, the original major stress is reduced to match the intermediate stress (29 MPa). Finally, in the mid-stress model, the original major stress is reduced halfway down to the intermediate. The ERR for each mining step with the different stress regimes is provided in Fig. 7.

Furthermore, it is useful to divide the stopes into two categories: hanging wall stopes and footwall stopes, where the hanging wall stopes are at the hanging wall contact, while the footwall stopes are at the footwall contact. Due to the mining sequence, all footwall stopes are in the stress shadow of a mined and backfilled hanging wall stope at their extraction time. The effect of the stope stress shadow is apparent in Fig. 7, where the ERR of the hanging wall stopes is significantly higher than the footwall stopes. The performance of destressing is therefore contingent on the ERR change for the hanging wall stopes rather than the footwall stopes. The hanging wall stopes are shaded in Fig. 7. The figure shows that the magnitude of the major stress has a significant effect on the ERR of the hanging wall stope extraction steps. Furthermore, given these stopes contribute to most of the cumulative ERR, the cumulative ERR of the entire pillar extraction sequence is significantly reduced with decreasing major stress. On the other hand, the footwall stopes are relatively unaffected by varying far-field stress conditions, given that the far-field stress for these stopes is cut-off by a hanging wall stope at the time of extraction.

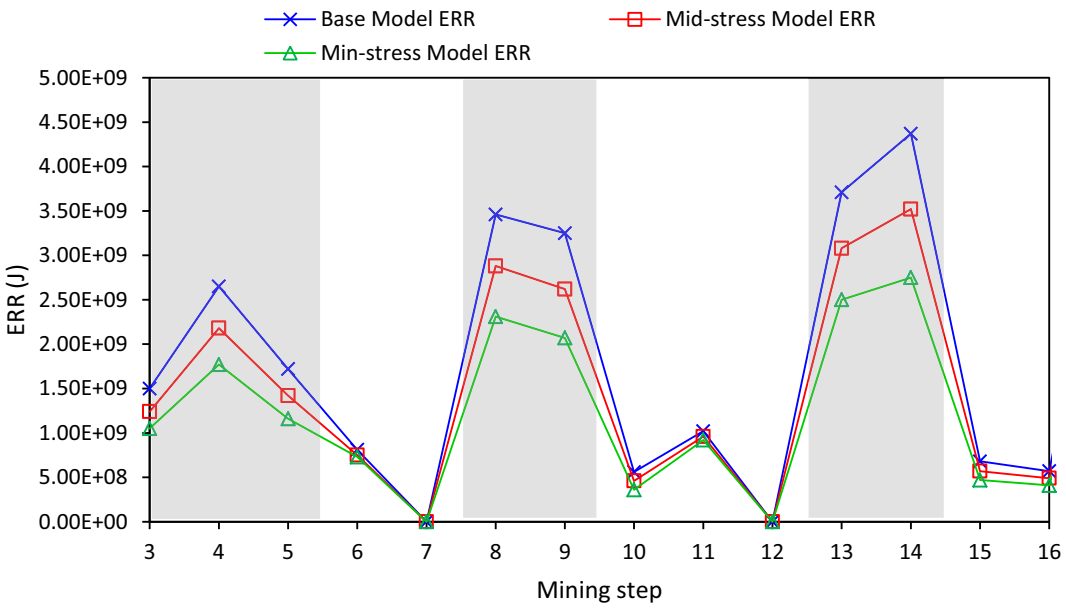

Fig. 7. Mining sequence ERR for different far-field loading scenarios. Hanging wall (primary) stope extraction steps are shaded in grey.

3.2. Effect of base destressing scheme

The base destressing scheme (thickness = 3 m, standoff = 3 m, overhang = 1 m) was implemented in the base loading model, and the ERR of each mining step and destressing step was recorded. Fig. 8 shows a comparison between the base destressing scheme step ERR and the ERR of the steps in the extraction sequence with no destressing. A similar response to reducing the major far-field stress is apparent. The hanging wall stopes experience a significant decrease of their extraction ERR, while the footwall stopes are relatively unaffected.

Fig. 9 superposes the step ERR range from Fig. 7 with the ERR of the base destressing sequence. The figure demonstrates that the ERR reduction due to destressing manifests itself in a similar fashion to the ERR reduction due to far-field stress reduction. The reduction of ERR due to destressing can be therefore equated to an equivalent major principal stress change. This value is linearly interpolated

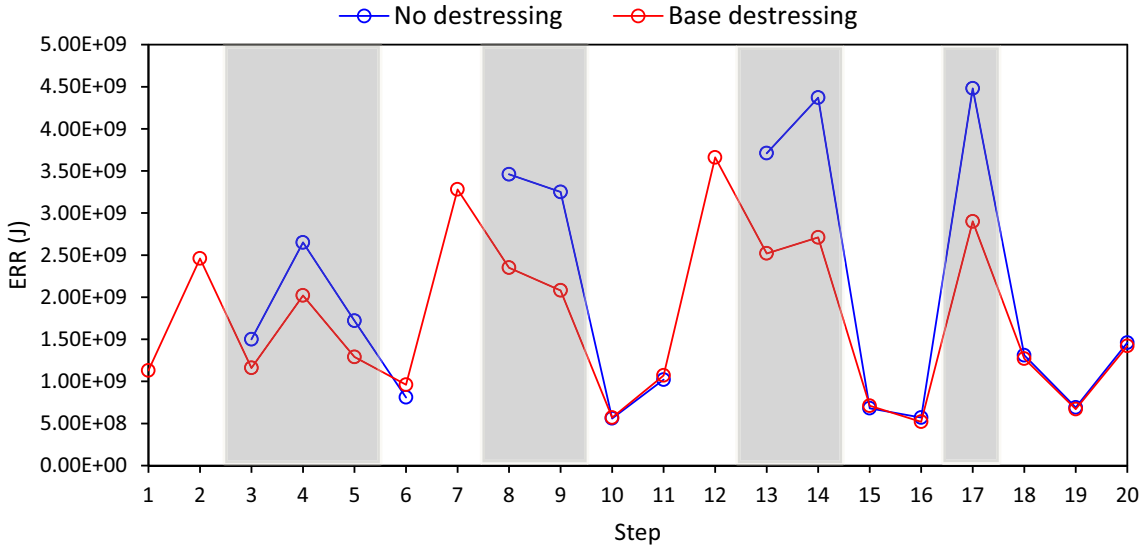

Fig. 8. Mining sequence ERR for base destressing model and model with no destressing. Far-field stress regime is equal in both models (base stress). Hanging wall (primary) stopes are shaded in grey.

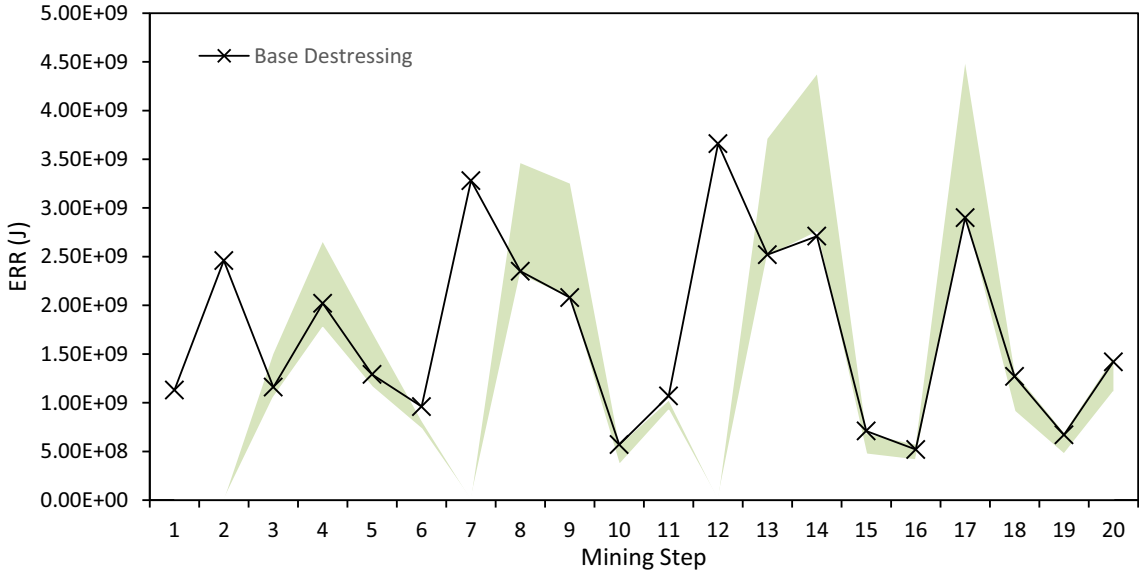

Fig. 9. Base destressing scheme ERR superposed on ERR range for tested far-field stress regimes. The ERR range is shaded in grey. The upper bound is set by the base stress model. The lower bound is set by the min-stress model.

based on the bounds plot in Fig. 7. For example, the ERR of steps 8 and 9 is equal to the lower bound defined by the min-stress model, where major far-field stress is reduced by 10 MPa with respect to the base model. Therefore, the equivalent major stress change for steps 8 and 9 of the base destressing model is roughly equal to −10 MPa. The exact values are determined with linear interpolation between the far-field stress model ERR bounds.

Fig. 10 shows the ERR of the mining sequence with base destressing along with the equivalent major principal stress change due to base destressing. Overall, the base destressing scenario reduces the stope extraction ERR by 3–40%, which is equivalent to a major stress reduction between 0.9 and 10.5 MPa. Furthermore, the figure shows that destressing has a significant effect on the hanging wall stopes. The equivalent stress changes due to destressing ranges between −7 MPa and −10 MPa. Considering that the virgin far-field stress in the base model is 51 MPa, the equivalent far-field stress change represents a 14–20% reduction in the major stress. In effect, by cutting off the major principal stress, the base destressing scheme reduced the

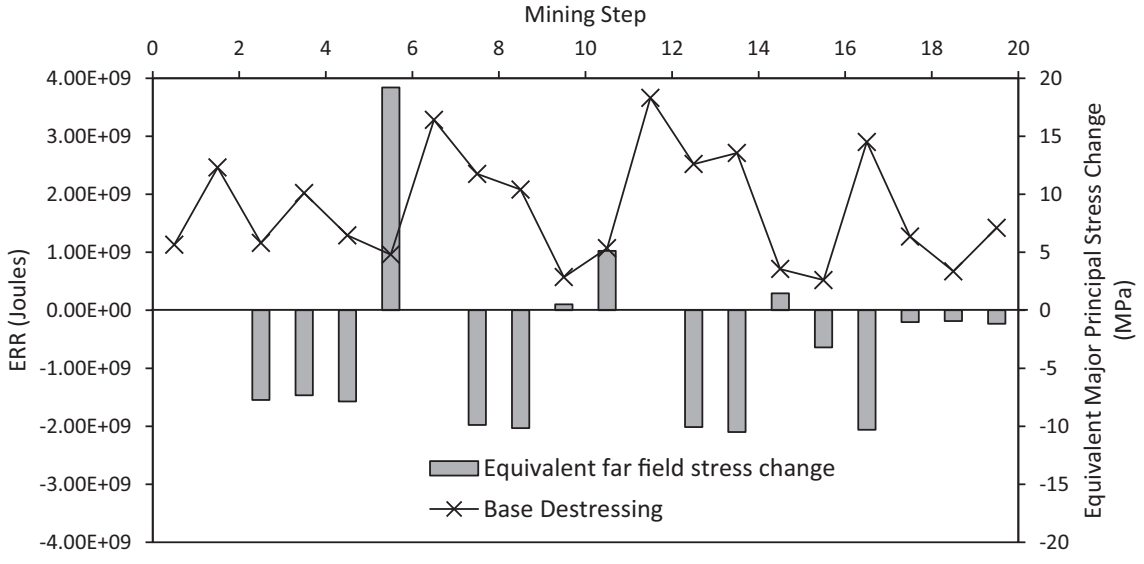

Fig. 10. Base destressing sequence ERR with interpolated equivalent far-field stress changes for all mining steps.

major principal stress in the pillar down to the magnitude of the intermediate principal stress.

3.3. Effect of panel geometry

The effect of geometric parameters is first evaluated with the two extreme factorial point models. The first model is the combination of the lowest standoff, highest thickness, and highest overhang, all of which contribute to a high destressing effect (standoff = 2 m, thickness = 4.5 m, overhang = 2 m). The second model has the combination yielding the lowest destressing effect (standoff = 4 m, thickness = 1.5 m, overhang = 0 m). Fig. 11 plots the ERR change of all mining steps for the two extreme factorial point models and the base destress model. The figure shows a clear relation between the panel ERR and the ERR change for the stopes. For the extreme factorial model with the highest destressing effect (in red), both a higher panel blasting ERR, as well as a higher ERR reduction for the stopes, is obtained. The low destressing effect factorial model has the opposite effect, providing the lowest ERR reduction for the stopes, and the lowest panel ERR.

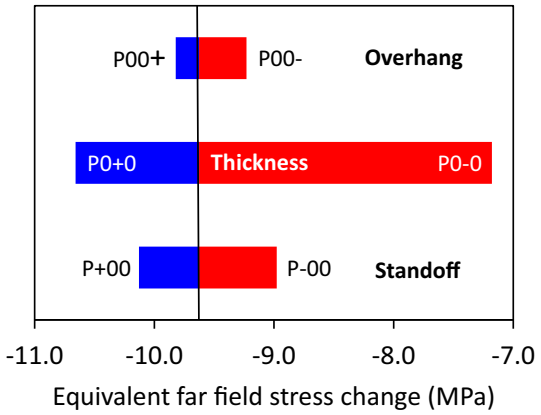

Fig. 12. Equivalent far-field stress change yielded by star–point models.

Next, the star point models were analysed to isolate the effect of each geometric parameter. With these models, two parameters are kept at their base value, while one is varied between two extremes.

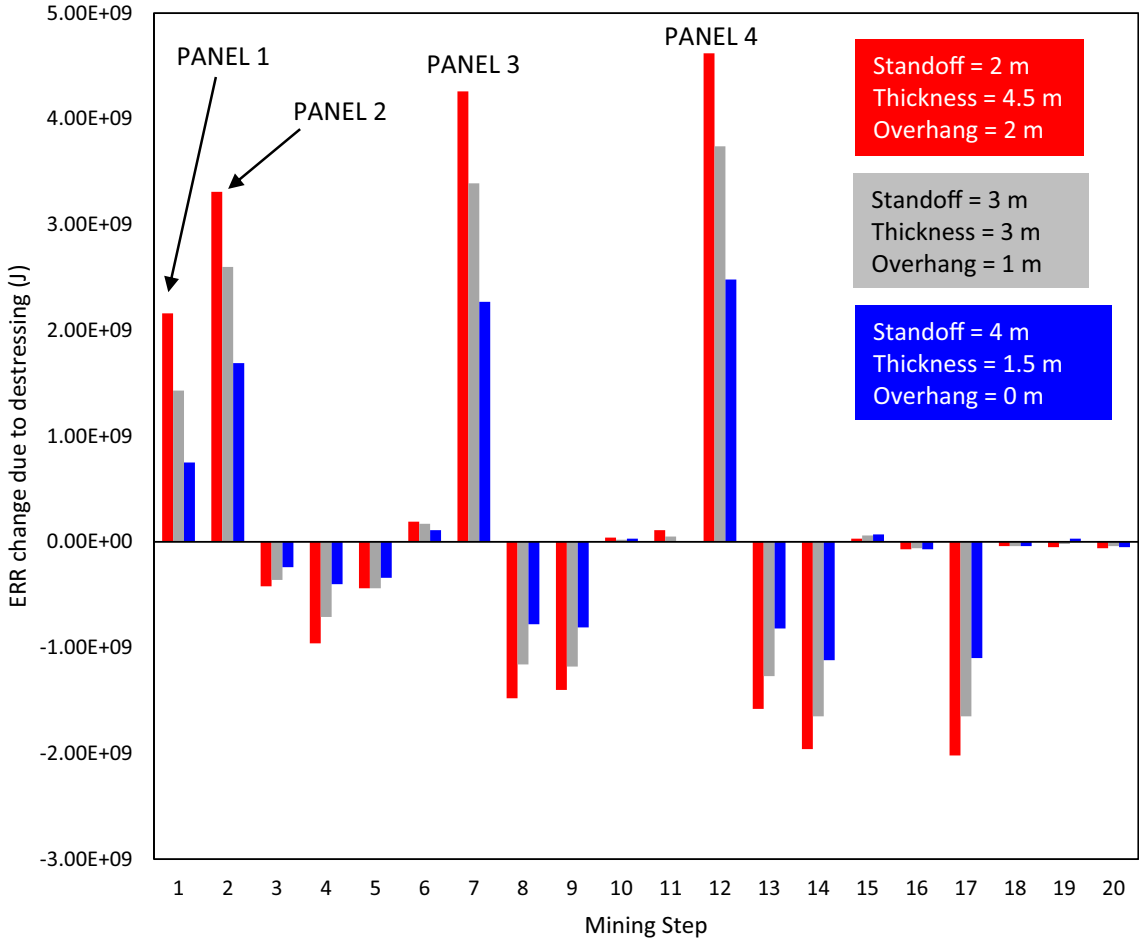

Fig. 11. Model ERR change with respect to the base model with no destressing for all mining steps.

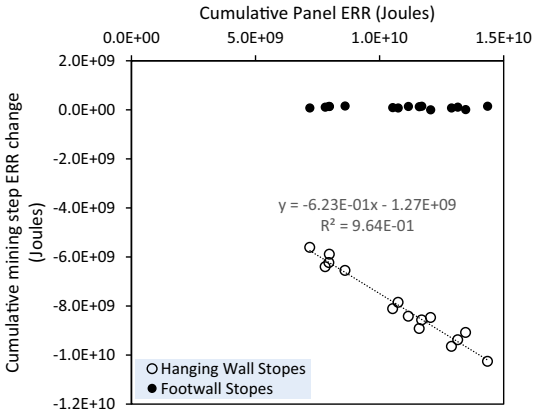

Fig. 13. Stope extraction sequence ERR change relative to cumulative panel ERR.

The equivalent major stress change is then calculated based on the ERR reduction. Fig. 12 shows the six resulting equivalent far-field stress changes calculated from the star point models. First, it is shown that the base model provides an equivalent major far-field stress of −9.6 MPa, signifying a substantial drop in pillar stresses. Moreover, increasing the thickness to 4.5 m from the base model provides the highest benefit, with the equivalent major stress further decreasing to −10.6 MPa. Conversely, decreasing the thickness down to 1.5 m provides the least overall benefit. It is therefore apparent that the most sensitive geometric parameter is the thickness. The next most crucial parameter for the effectiveness of destressing is the stand-off distance. The least crucial is the overhang.

Finally, Fig. 13 plots the cumulative ERR reduction for stope extraction with respect to the cumulative panel ERR for all parametric study models. There is a clear linear trend between the panel ERR and the reduction of ERR provided to the hanging wall stopes. The ratio is approximately 60%, signifying that to obtain a 0.6 J reduction of ERR when mining, a 1 J ERR increase is required in the form of destressing. The overall cumulative ERR of a sequence will always be higher than one without assuming a linear-elastic model. The figure also shows the negligible effect destressing has on the footwall stopes. In fact, these stopes are within the stress shadow of the mined and backfilled hanging wall stopes at their time of extraction. The effect of the panel on these stopes is therefore suppressed.

3.4. Copper Cliff Mine

Copper Cliff Mine (CCM) is an underground hard rock metal mine located in Copper Cliff near Sudbury, Ontario, Canada. The mine is currently operated by Vale Canada Ltd and exploits multiple orebodies. Extraction of a large remnant pillar in 100OB with the assistance of a large-scale panel destressing program began in 2014 [11].

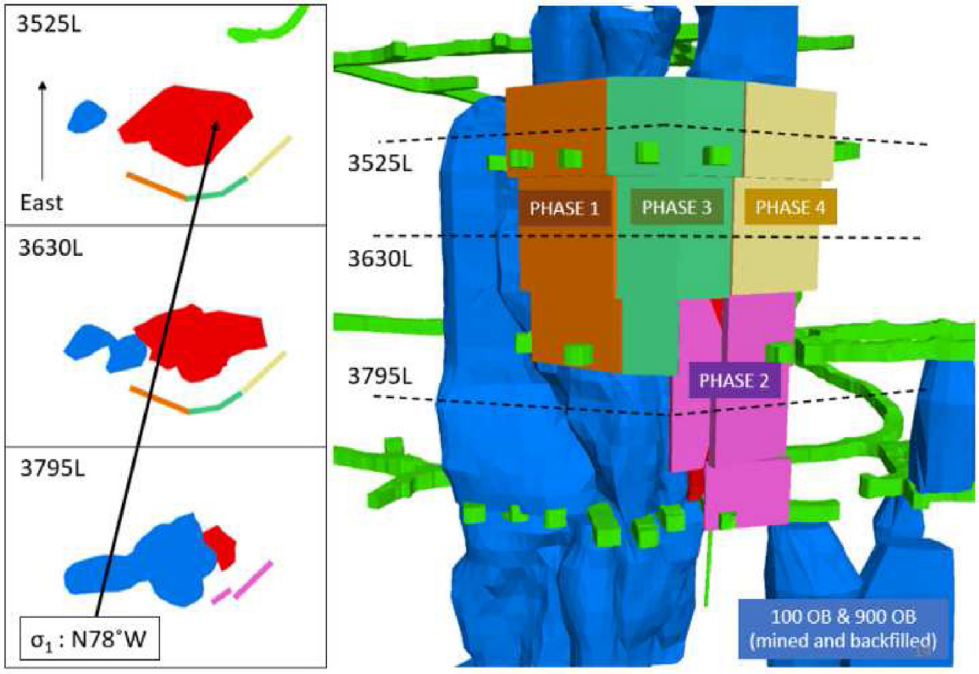

Fig. 14. CCM panel destressing program [11].

3.5. Destress blasting program

The aim of the destress blast program implemented at CCM was to create a stress shadow which encompasses all the stopes in the 100OB diminishing ore pillar. Sill drifts on multiple levels were extended into the hanging wall, from which rings of blastholes parallel to the orebody strike were drilled to form a series of panels which completely shield the diminishing ore pillar. These panels are destressed in four phases as mining of the diminishing ore pillar progresses, as shown in Fig. 14.

The numerical developed described by Vennes et al. [11] is employed in this study. The same rock fragmentation and stress reduction factors are applied in the case study model and the parametric study model ($\alpha = 0.05, \beta = 0.95$). The entire pillar is destressed and extracted in proper sequence and the ERR of each mining step and destressing step is calculated.

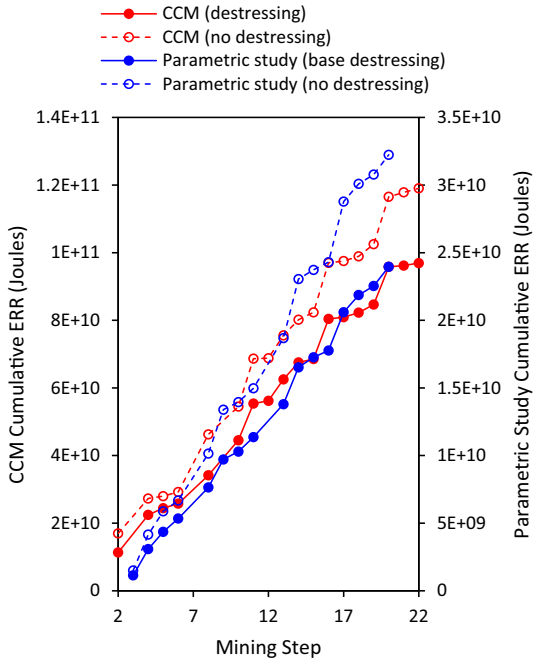

Fig. 15. Cumulative stope extraction ERR for parametric study and CCM.

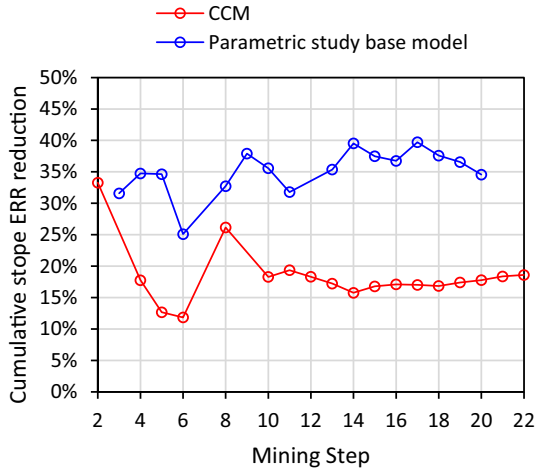

Fig. 16. Reduction of cumulative stope extraction ERR due to destressing.

3.6. Mining sequence ERR

Fig. 15 shows the cumulative ERR obtained for the CCM pillar extraction sequence and the parametric study pillar extraction sequence. The base destressing scheme is applied in the parametric study model, and the original panel geometry is used in the CCM model. Overall, the CCM cumulative stope extraction ERR with destressing and without destressing rate is higher than the parametric study cumulative ERR due to its higher volume. In both cases, destressing reduces stope extraction cumulative ERR. Fig. 16 shows the relative reduction of stope ERR due to destressing. For the parametric study, base destressing provides an overall ERR reduction of 35% once all stopes are extracted. In the case of CCM, the destressing program decreases the cumulative ERR by 19%.

4. Conclusions

The effect of panel geometry on the ERR of the mining sequence was quantified in a 3D numerical modelling parametric study. The study shows that the panel thickness has the most effect on the ERR, followed by the panel stand-off and the panel overhang. The study also demonstrates that the ERR reduction experienced by the stopes is directly proportional to the ERR of the panels, where the ratio is 60%. This signifies that the cumulative sequence ERR with destressing will be higher than without destressing, although the cumulative ERR of stope extraction is reduced. Also, the equivalent major principal stress change provided by destressing was calculated for all models. The base destressing scheme is shown to reduce the ERR to the same level as a 9.6 MPa reduction of the major stress. Finally, the ERR of each mining step of the remnant pillar at CCM was calculated in a scenario with and without destressing. The benefit of the destressing sequence is apparent. The stress shadow generated by destressing the panel with validated destress blasts parameters $\alpha = 0.05$ and $\beta = 0.95$ reduces the mining sequence ERR by 20% overall. For the parametric study base model, the reduction is 35%. Further investigation on the effect of far-field stress orientation and pillar geometry is required to explain the discrepancy fully.

Ethical statement

The authors state that the research was conducted according to ethical standards.

Funding body

This work was financially supported by a research grant from NSERC Discovery Grant No. 05645.

Conflicts of interest

The authors declare no conflict of interest.

References

[1] Blake W. Destressing test at the galena mine. Trans SME-AIME 1972;252(1):294–9.
[2] Tang B, Mitri HS. Numerical modelling of rock preconditioning by destress blasting. Ground Improv 2001;5:1–11.
[3] Saharan MR, Mitri HS. Simulations for rock fracturing by destress blasting, as applied to hard rock mining conditions. Saarbrucken: VDM Verlag; 2009.
[4] Zhu WC, Wei CH, Li S, Wei J, Zhang MS. Numerical modeling on destress blasting in coal seam for enhancing gas drainage. Int J Rock Mech Min Sci 2013;59:179–90. https://doi.org/10.1016/j.ijrmms.2012.11.004.
[5] Sainoki A, Emad MZ, Mitri HS. Study on the efficiency of destress blasting in deep mine drift development. Can Geotech J 2017;54(4):518–28. https://doi.org/10.1139/cgj-2016-0260.
[6] Baranowski P, Damaziak K, Mazurkiewicz Ł, Mertuszka P, Pytel W, Małachowski J, et al. Destress blasting of rock mass: multiscale modelling and simulation. Shock Vib 2019;2019. https://doi.org/10.1155/2019/2878969.
[7] Yu S, Yang X, Zhu C, Yuan Y, Wang Z. Destressing mechanics effect of surrounding rock induced by blasting precondition at deep drift development. Geotech Geol Eng 2021;39(6):4113–25. https://doi.org/10.1007/s10706-021-01687-1.
[8] Vennes I, Mitri H. Geomechanical effects of stress shadow created by large-scale destress blasting. J Rock Mech Geotech Eng 2017;9(6):1085–93. https://doi.org/10.1016/j.jrmge.2017.09.004 (license CC BY-NC-ND 4.0. https://creativecommons.org/licenses/by-nc-nd/4.0/.
[9] Andrieux P, Brummer R, Mortazavi A, Liu Q, Simser BP. Large-Scale panel destress blast at Brunswick Mine. Cim Bull 2003;96:78–87.
[10] Andrieux P. Application of rock engineering systems to large-scale confined destress blasts in underground pillars. Laval University; 2005. Department of Mining, Metallurgical, and Material Sciences. [Quebec].
[11] Vennes I, Mitri H, Chinnasane DR, Yao M. Large-scale destress blasting for seismicity control in hard rock mines: a case study. Int J Min Sci Technol 2020;30(2):141–9. https://doi.org/10.1016/j.ijmst.2020.01.005 (license CC BY-NC-ND 4.0: https://creativecommons.org/licenses/by-nc-nd/4.0/.
[12] Vennes I, Mitri H, Chinnasane DR, Yao M. Effect of stress anisotropy on the efficiency of large-scale destress blasting. Rock Mech Rock Eng 2021;54(1):31–46. https://doi.org/10.1007/s00603-020-02252-7.
[13] Shnohorkian S, Mitri HS, Moreau-Verlaan L. Stability assessment of stope sequence scenarios in a diminishing ore pillar. Int J Rock Mech Min Sci 2015;59.
[14] Mitri HS, Tang B, Simon R. FE modelling of mining-induced energy release and storage rates. J South African Insitute Min Metall 1999:103–10.
[15] Drover C, Villaescusa E. A comparison of seismic response to conventional and face destress blasting during deep tunnel development. J Rock Mech Geotech Eng 2019;11(5):965–78. https://doi.org/10.1016/j.jrmge.2019.07.002.
[16] Wojtecki Ł, Konicek P, Mendecki MJ, Zuberek WM. Evaluation of destress blasting effectiveness using the seismic moment tensor inversion and seismic effect methods. Int J GeoMech 2022;22(4):1–11. https://doi.org/10.1007/s00603-017-1297-9.
[17] Fuławka K, Mertuszka P, Pytel W, Szumny M, Jones T. Seismic evaluation of the destress blasting efficiency. J Rock Mech Geotech Eng 2022. https://doi.org/10.1016/j.jrmge.2021.12.010.
[18] Wojtecki Ł, Mendecki MJ, Gołda I, Zuberek WM. The seismic source parameters of tremors provoked by long-hole destress blasting executed during the longwall mining of a coal seam under variable stress conditions. Pure Appl Geophys 2020;177(12):5723–39. https://doi.org/10.1007/s00024-020-02603-z.
[19] Castro LAM, Grabinsky MW, McCreath DR. Damage initiation through extension fracturing in a moderately jointed brittle shear rock mass. Int J Rock Mech Min Sci 1997;34:110–3.
[20] Konicek P, Waclawik P. Stress changes and seismicity monitoring of hard coal longwall mining in high rockburst risk areas. Tunn Undergr Space Technol 2018;81:237–51. https://doi.org/10.1016/j.tust.2018.07.019.
[21] Cook NGW, Heok E, Pretorius JPG. Rock mechanics applied to the study of rockbursts. J South African Inst Min Metall 1966;66:93.
[22] Qinghua X, Jianguo L, Shenxiang L, Bo G. A new method for calculating energy release rate in tunnel excavation subjected to high in situ stress ☪. Perspect Sci 2016;7:292–8. https://doi.org/10.1016/j.pisc.2015.11.045.
[23] Wang W, Cheng Y, Tan G. Design Optimization of SBS-modified asphalt mixture reinforced with eco-friendly basalt fiber based on response surface methodology. Materials 2018;11(8). https://doi.org/10.3390/ma11081311 (license CC BY 4.0. https://creativecommons.org/licenses/by/4.0/.